Monitoring the seasonal dynamics of soil salinization in the Yellow River Delta of China using Landsat data

Hongyan Chen[*], Gengxing Zhao, Yuhuan Li, Danyang Wang, Ying Ma

National Engineering Laboratory for Efficient Utilization of Soil and Fertilizer Resources, College of Resources and Environment, Shandong Agricultural University, Taian 271018, China

[*]Corresponding author: Hongyan Chen, College of Resources and Environment, Shandong Agricultural University, No.61 Daizong Street, Tai'an, Shandong 271018, PR China. E-mail: chenhy@sdau.edu.cn

Abstract. It is necessary to monitor the seasonal dynamics of soil salinization in regions with distinct seasonal climates. The article took Kenli district in the Yellow River Delta (YRD) of China as the experimental area. Based on Landsat data from spring and autumn, improved vegetation indices (IVIs) were created, which were then applied to the inversion modeling of soil salinity content (SSC) by employing stepwise multiple linear regression, back propagation neural network and support vector machine methods. Finally, the optimal SSC model in each season was extracted, and the spatial distributions and seasonal dynamics of SSC in a year were analyzed. The results indicated that the SSC varied obviously between seasons in the YRD, and the support vector machine method resulted in the best inversion models. The best SSC inversion model for spring could be applied to the SSC inversion in winter; similarly, the best model for autumn could also be applied to SSC inversion in summer. The SSC exhibited a gradually increasing trend from southwest to northeast in Kenli district, and it also underwent the following seasonal dynamics: soil salinity accumulates in spring, decreases in summer, increases in autumn, and peaks in winter. This work provides data support for the treatment and utilization of saline-alkali soil in the YRD.

Keywords: Soil salinity; Remote sensing inversion; Vegetation index; Multispectral imaging; Seasonal dynamics

1. Introduction

Saline soils, which are widespread throughout the world, especially in arid, semiarid and some subhumid regions, cause severe environmental degradation that can impede crop growth as well as overall regional production (Metternicht and Zinck 2003).

5 Moreover, as a form of land degradation, soil salinization can degrade soil quality and lead to ecosystem risks (Huang et al. 2015; Zhao et al. 2018). Obtaining information on soil characteristics, such as the degree of salinity and geographical distribution of saline soil in real time, and improving our ability to forecast soil salinization dynamics are necessary prerequisites for scientific management, reasonable improvement and

10 utilization of regional saline soil, then help to reduce ecological risks (Melendez-Pastor et al. 2012; Yang et al. 2018). Remote sensing technology provides an important and rapid approach for the quantitative monitoring and mapping of soil salinization (Dehni and Lounis 2012; Tayebi et al. 2013; Shoshany et al. 2013; Sidike et al. 2014; Wu et al. 2014; Guo et al. 2015; Sturari et al. 2017).

Multispectral satellite data, such as Landsat, SPOT, IKONOS, QuickBird, and the Indian Remote Sensing (IRS) series of satellites, have been used to map and monitor soil salinity and other properties due to the low cost and the ability to map extreme surface expressions of salinity (Dwivedi et al. 2008; Abbas et al. 2013; Allbed et al.

20 2014; Mahyou et al. 2016; Mehrjardi et al. 2008; Yu et al. 2010; Ahmed and Iqbal 2014; Rahmati and Hamzehpour 2016). Extensive studies have shown that models based on multispectral satellite data are still the preferred method for mapping soil salinity over large spatial domains (Allbed and Kumar 2013; Scudiero et al. 2015; Taghizadeh-Mehrjardi et al. 2014).

To a certain extent, information on the damage to vegetation caused by soil

salinization can help to determine the degree and trend of soil salinization. Therefore,

traditional vegetation indices (VIs), such as the normalized difference vegetation index

(NDVI), the ratio vegetation index (RVI), and the difference vegetation index (DVI),

can be used as indicators to determine the degree of soil salinization (Elmetwalli et al.

2012; Li et al. 2013; Goto et al. 2015). However, the accuracy of the models based on

traditional VIs must be improved (Iqbal 2011). Traditional VIs involve the data from

only two bands in the visible and near-infrared region, and there are often significant

correlations between traditional VIs (USGS, 2013). Therefore, it is worth studying

whether the addition of data from the shortwave infrared band, which has long

wavelengths and contains considerable information, can improve the accuracy and

stability of soil salinity content (SSC) inversion models.

Existing studies primarily focus on SSC inversion models for a single study area at

a specific time (Herrero and Casta ñeda 2015; He et al. 2014); nevertheless, because the

SSC is dynamic over time, such as through the four seasons of a year, the application of

the same inversion model to quantitatively analyze the SSC in different seasons is not

adequate. The Yellow River Delta (YRD) is located at the junction of the Beijing-

Tianjin-Hebei metropolitan area and Shandong Peninsula and lies within the efficient

ecological economic zone of China, and this region has obvious geographical

advantages. With nearly 550,000 ha of unused land, the land resources in this area are

rich. However, soil salinization is a widespread and serious concern in this region (Mao

et al. 2014). Approximately 85.7% of the total area in the region is covered with saline

soil, and there has been an increasing trend in the amount of coastal saline soil in recent

years. As the main risk to farmland ecosystems in this region, soil salinization can result in a large reduction in agricultural production and fragile ecological environments; and, soil salinization seriously affects the utilization of land resources as well as the development of the regional economy and society (Yang et al. 2015; Weng et al. 2010).

5 Moreover, in regions with distinct seasons, the differences in rainfall and evaporation between different seasons are great, the changes in soil moisture are obvious, and soil salinity exhibits a close relation with soil moisture; thus, the soil salinity usually varies greatly between seasons. Therefore, it is particularly necessary to monitor the seasonal dynamics of soil salinization in this region. Seasonal SSC inversion models would

10 greatly improve the accuracy of SSC modeling and therefore enhance our ability to monitor soil salinization in the region continuously and in real time.

The objectives of this paper are to (1) build optimal SSC inversion models for different seasons according to soil salinity conditions; (2) map the spatial distribution

15 and seasonal dynamics of SSC in the YRD of China. Specifically, VIs were constructed by introducing data from the shortwave infrared band (SWIR) of Landsat data. The SSC inversion models in spring and autumn were built using stepwise multiple linear regression (SMLR), back propagation neural network (BPNN) and support vector machine (SVM) methods, and the best models for spring and autumn were

20 selected and applied to the other seasons. Once the optimal soil salinity inversion model was determined for each season, it was applied to map the SSC distribution and analyze the seasonal SSC dynamics.

2. Materials and methods

2.1 Study area

The study area is the Kenli district in the YRD region (37°24′~38°06′N, 118°14′~119°11′E), which is located in Dongying city, Shandong Province, China, and on the southern shore of the Bohai Sea (Fig. 1). This area has a characteristic plain landscape and coastal saline soil type. There are three types of soil subgroups: tidal soil, salinized tidal soil and coastal tidal saline soil. The soil parent material is the Yellow River alluvial material, and the soil texture is light; salt accumulates on the soil surface, and salt is relatively rare and well-distributed in the middle and lower parts of the soil profile (below the core soil). The main types of land use in this area are cultivated land, unused land and grassland. The main crops are wheat, corn, rice and cotton. The main natural vegetation includes white grass, reed, horse trip grass, tamarix and suaeda. Owing to the low, flat terrain, high groundwater table, high mineralization rate, poor drainage conditions, and the infiltration and mounting of seawater associated with the Yellow River in this region, soil salinization at the surface is generally severe and widespread (Yang et al. 2015; Weng et al. 2010). Due to the temperate climate and four distinct seasons, the soil salt content exhibits obvious seasonal dynamics. The soil salinization process in the region is shown in Fig. 2.

2.2 Soil sampling and chemical analyses

To achieve an accurate representation of the seasonality, we selected April, August, November and February (in the following year) to represent the spring, summer, autumn, and winter seasons, respectively. According to the climate characteristics and soil salinization conditions in the different seasons, the samples collected in spring and

autumn were used to develop the SSC inversion models, while the samples from winter

and summer were used to validate the inversion models. Overall, 92 spring samples

were collected from April 27-May 2, 2013; 30 summer samples were collected from

August 14-15, 2013; 110 autumn samples were collected from November 9-13, 2013;

5   and 56 winter samples were collected from February 26-29, 2014. Sample points were

designated by considering the degree of soil salinization, soil surface morphology and

microtopography, and uniformity of the sample distribution (Fig. 1). Topsoil samples

were collected at each sample point at a depth < 20 cm, and GPS coordinates were

recorded. *In situ* environmental information was also recorded. The collected soil

10   samples were naturally air dried, crushed, purified, passed through a 2 mm sieve, and

mixed evenly. The concentrations of Cl^-, SO_4^{2-}, CO_3^{2-}, HCO_3^-, K^+, Na^+, Ca^{2+}, and Mg^{2+}

were measured in extracted solutions of a 1:5 soil-water mixture. The SSC was defined

as the combined concentration of the eight ions mentioned above.

15   *2.3 Acquisition and pretreatment of imaging data*

Multispectral Landsat data were acquired in line with the sample collection time. We

employed Landsat 7 ETM+ data from May 6, 2013, and Landsat 8 OLI data from

August 18, 2013, November 6, 2013, and February 26, 2014. Landsat 7 ETM+ data

include one panchromatic band (520–900 nm), four multispectral bands in the visible

20   and near-infrared wavelength range (blue (450–515 nm), green (525–605 nm), red

(630–690 nm) and NIR (775–900 nm)), and two shortwave infrared (SWIR) bands

(1550–1750 nm, 2090–2350 nm). The Landsat 8 OLI data the same bands as ETM+,

while the band ranges are slightly different. Image pretreatment, including geometric

rectification, radiation calibration, and atmospheric correction, was conducted in ENVI

5.1 software from the Exelis Visual Information Solutions. Geometric rectification was completed in reference to the 1:10000 terrain map of the study area, and then radiation calibration and Fast Line-of-Sight Atmospheric Analysis of Spectral Hypercubes (FLAASH) atmospheric correction were subsequently applied. The output images were

5   projected to the Gauss–Kruger coordinate system and cropped to the study area. Then, the water body, building and traffic land areas were masked according to the current land use situation. Finally, the reflectance of the samples was extracted from the processed images using ArcGIS 10.1 software.

10   *2.4 Calculation and improvement of vegetation indices*

The extended vegetation indices (EVIs) were all calculated based on the Landsat data by adding the SWIR band data to the traditional VIs, including the extended normalized difference vegetation index (ENDVI, (NIR+SWIR-R)/(NIR+SWIR+R)), extended difference vegetation index (EDVI, NIR+SWIR-R), and extended ratio

15   vegetation index (ERVI, (NIR+SWIR)/R). The SWIR band refers to either of the two SWIR bands. The correlations between the SSC and EVIs were analyzed, and then the EVIs with significant correlation coefficients were selected as the improved vegetation indices (IVIs). Finally, the IVIs were used as the inputs to the SSC inversion models.

20   *2.5 Inversion model construction and optimization*

First, soil samples collected in spring and autumn were sorted and separated according to the SSC. Two-thirds of the samples were chosen for the calibration set, and the remaining samples were used as the validation set. Therefore, of the 92 samples collected during spring, 62 samples were used for calibration, and the other 30 samples

were used for validation. Similarly, of the 110 samples collected during autumn, 74

samples were used for calibration, and the other 36 samples were used for validation.

Second, the SSC inversion model for spring was built by employing the SMLR, BPNN

and SVM methods based on the VIs and corresponding IVIs. The performance of the

5 SSC inversion models was evaluated by the coefficient of determination (R^2), root-

mean-square error (RMSE) and ratio of performance to deviation (RPD). Using the

same procedures, the SSC models for autumn were built on the IVIs, and the best model

was selected. Finally, the best models for spring and autumn were selected and applied

to the summer and winter data, and then the optimal SSC inversion models according to

10 the soil salinization conditions in different seasons were selected.

For the SMLR method, the variance inflation factor (VIF) was set to less than 5 to

control multicollinearity. The BPNN method was conducted using the MATLAB

R2012a program. During the calculation, the transfer functions of the hidden layer and

15 the output layer were set to tansig and logsig, respectively. The network training

function was traingdx, and the learning rate, the maximum training time, and the model

expectation error were set to 0.01, 15000, and 0.01, respectively. The SVM models

were built in the Libsvm 3.11 toolbox in MATLAB R2012a. In this model, we selected

the 4th SVM type (v-SVR) and the 2nd kernel function (RBF), and the penalty

20 parameter C and the kernel parameter g of the RBF were determined according to the

minimum mean-squared deviation by using the cross-validation and grid search method.

2.6 SSC distribution mapping and year-round dynamics analysis

The reflectance spectra were extracted from the Landsat data from the four seasons in the study area, and the seasonal IVIs were calculated. Then, the SSC distribution maps of the four seasons were obtained via calculations based on the corresponding optimal models. The spatial distribution characteristics and seasonal dynamics of soil salinity in the YRD were analyzed and compared.

The methodological flow of this article is shown in Fig. 3.

3. Results

3.1 The soil samples data

The statistical results of the SSC samples from the four seasons (the upper half of Table 1) showed that the SSC in the study area remained high with a mean > 5.32 g/kg throughout the year. As determined from the minimum, maximum, and mean values, our results showed that the SSC reached its maximum concentration in winter (the mean = 9.50 g/kg) and decreased gradually, and the SSC varied obviously between seasons. The standard deviation and coefficient of variation showed that the SSC gradient was significant overall, especially in winter and spring.

3.2 Improved vegetation indices (IVIs)

In spring, the correlation coefficients between the EVIs and the SSC of the soil samples were -0.52 for ENDVI, -0.69 for ERVI and -0.70 for EDVI; similarly in autumn, the

correlation coefficients between the EVIs and the SSC of the soil samples were -0.73

for ENDVI, -0.69 for ERVI and -0.69 for EDVI.

The results show that the correlation coefficients between the ERVI or EDVI and

5   SSC were very significant (R^2>0.69; P<0.01) in spring. Based on these findings,

ERVI and EDVI were selected as the IVIs for spring, while ENDVI and ERVI were

selected as the IVIs for autumn. For each season, the chosen IVIs and their

corresponding VIs were used to build the SSC inversion models.

10   *3.3 The best SSC inversion models and their application to different seasons*

3.3.1 SSC inversion models with VIs and IVIs

The results of the SSC inversion models in spring based on the IVIs are shown in

Table 2. The performances of the three modeling methods were compared, which

showed that the prediction accuracy of the SVM models was the highest followed by

15   the BPNN models, and the SMLR models had the lowest accuracy. In terms of the

calibration values, the SVM models based on the IVIs had the best and most stable SSC

inversion accuracies for both the calibration set (R^2> 0.72, RMSE <6.34 g/kg) and the

validation set (R^2 > 0.71, RMSE <6.00 g/kg, and RPD >1.66). These models were then

selected as the best SSC inversion models for the SSC in spring and autumn.

The calibration and validation precision of the SSC inversion models in spring and

autumn are shown in Fig. 4.

3.3.2 Application of the best SSC inversion models with IVIs in different seasons

The best *SSC* inversion models for spring and autumn were applied to the SSC estimation of summer and winter, respectively. Based on the estimation accuracy (Table 3), the best SSC inversion model for spring can be applied to that in winter, with R^2 of

5   0.66 and RMSE of 7.57 g/kg. Meanwhile, the best SSC inversion model for autumn can also be applied to that in summer, resulting in R^2 of 0.65 and RMSE of 3.60 g/kg. In response to the soil salinity conditions, the SSC inversion model for spring based on the IVIs in combination with the SVM method was selected as the optimal SSC model for spring and winter, while the SSC inversion model for autumn based on the IVIs in

10   combination with the SVM method was selected as the optimal SSC model for autumn and summer in the YRD.

3.4 Distribution and seasonal dynamics of SSC in the YRD region

3.4.1 Distribution of SSC in four seasons

15   Based on the processed Landsat data and the optimal SSC inversion model for each season, the SSC inversion maps in the four seasons were obtained. The descriptive statistics of the inversed SSC in four seasons are shown in the lower half of Table 1, which are close to those of the collected samples (the upper half of Table 1); the inversion results also showed that the SSC in winter was highest, followed by that in

20   spring, and the SSC in autumn and summer were relatively low.

According to the classification standard of coastal saline soil in the semihumid area of China, the study area was divided into 5 grades of soil salinization: nonsaline soil, mild saline soil, moderate saline soil, severe saline soil, and solonchak, with the degree

of soil salinization gradually increasing from nonsaline soil to solonchak. The distributions of the soil salinity grades in the four seasons were mapped (Fig. 5) and showed similar characteristics. There was a gradually increasing trend of soil salinity from southwest to northeast in the study region. The main reason for this gradual

5   increase in SSC is that the terrain of the southwest part of the study area is high and flat, and the flood-prone land is used for agricultural production. The central part of the region, near the banks of the Yellow River, has alternating hillocks, slopes and depressions, which were formed by the repeated diversion of the Yellow River; thus, each grade of soil salinization was also alternately distributed, and the northeast part of

10 the region, which has low terrain and is closest to the sea, has the most severe soil salinization.

3.4.2 Seasonal dynamics of SSC

The number of pixels and proportion of pixels per SSC grade were calculated for each

15 season (Table 4). Fig. 5 and Table 4 demonstrate that the SSC in the study area is clearly different among the four seasons. The SSC in spring consisted primarily of moderate saline soil, severe saline soil, and solonchak (combined proportion of 90.05%); in summer, the area of the four grades from the mild saline soil to solonchak was relatively uniform (each grade accounting for 22–28%); the SSC during autumn was

20 largely dominated by severe saline soil and solonchak (combined proportion of 77.75%); in winter, the SSC was principally severely saline and solonchak, with the combined proportion of 99.19%, of which the severe saline soil contributed 80.71%.

The seasonal SSC inversion values and the proportion of pixels per SSC grade indicated that the change in SSC between different seasons is relatively apparent. The degree of soil salinization was lowest in summer, and the SSC in autumn was relatively low except for the solonchak in coastal areas. In spring, the soil salinization became more obvious, with most of the study area belonging to the moderate to severe saline soil and solonchak group. Meanwhile, the soil salinization was the most severe in winter. In summary, soil salinity in the study area usually accumulates in spring, decreases in summer, increases in autumn, and peaks in winter.

4. Discussion

In this work, we introduced the SWIR band and proposed an improved vegetation index to increase the accuracy of SSC inversion models. The spatial distributions of SSC in the four seasons showed similar characteristics. There was a gradually increasing trend of soil salinity from southwest to northeast in the study region, and this distribution pattern is consistent with the results of other studies (Weng et al. 2010; Yang et al. 2015). Weng et al. (2010) also established an SSC remote sensing revision model using the data from 2153 ~ 2254 nm and 1941 ~ 2092 nm in the region of YRD and achieved good results.

We can see that the best SSC inversion models for spring and autumn are based on different IVIs. In spring, the weather is characteristically dry and windy with strong evaporation, and the coverage of natural vegetation is low; however, crops such as wheat and corn are in a vigorous growth stage, which results in strong vegetation

reflectance spectra. Generally, the RVI and DVI are sensitive to vegetation, especially

when vegetation coverage is high; thus, the inversion accuracies based on the ERVI and

EDVI are higher than those of other vegetation indices. In autumn, rainfall and

temperature are reduced, and there is little coverage of natural vegetation. At this time,

5   cotton has been collected, and only withered cotton leaves and rods remain in the field,

and wheat has just begun to emerge out of the soil. Therefore, the reflectance spectra of

vegetation are relatively weak in autumn. NDVI has low sensitivity to high vegetation

areas and is suitable for monitoring in low and moderate vegetation coverage areas, so

the inversion accuracies based on the ENDVI and ERVI are higher than those based on

10   the other vegetation indices. The results were obtained without considering some factors

(e.g., soil moisture and temperature) that vary with season and affect the SSC. The

influence of some key factors will be studied to remove these factors in future studies.

The seasonal dynamics of SSC are closely related to the climate of the study area.

15   With droughts, windy weather, and strong evaporation in spring from March to May,

soil salts aggregate at the soil surface as the soil moisture increases, which forms the

first peak of salt accumulation, with a total of 90.05% of moderate saline soil, severe

saline soil, and solonchak. Rainfall and floods occur in the summer from June to August,

and as precipitation infiltrates into the soil, the soil surface is desalinated, with a

20   uniform proportion from the mild saline soil to solonchak. In the autumn from

September to November, rainfall decreases and SSC increases slightly, and the area is

largely dominated by severe saline soil and solonchak (combined proportion of 77.75%).

Due to drought in winter from December to February, combined with decreased

evaporation, soil salinization is relatively severe and remains latent at the soil surface,

with 99.19% of the area covered by severe saline and solonchak. By the end of the

season, the SSC will reach the peak. Lu et al. (2016) presented that SSC exhibits

seasonal variation in the YRD and that the SSC in spring was higher than that in autumn

in the Kenli district, which is consistent with our results.

Based on the time point data, the results indicated that the SSC inversion model for

spring could be applied to SSC inversion in winter, while the SSC inversion model for

autumn could also be applied to SSC inversion in summer in the YRD. These model

selection results may be due to the short time intervals, similar soil salt contents and

10   climatic conditions between February and April and between August and November in

the YRD. To respond more accurately to the dynamic changes in soil salt, a period of

SSC data should be selected as the seasonal salt data, which will be further studied in

future research.

15   **5. Conclusion**

In this experiment, the results showed that the ERVI and EDVI were the IVIs for spring,

while the ENDVI and ERVI were the IVIs for autumn. These models based on the IVIs

that utilized the SVM method were selected as the best SSC inversion models for spring

and autumn. The experimental results contribute to the quantitative and accurate

20   monitoring of soil salinization with multispectral imaging and provide data and

technical support for saline soil management and utilization and ecological

environment protection.

This experiment indicates that the best inversion model for spring could be applied for the SSC inversion in winter, and the optimal SSC model for spring and winter was selected in response to the soil salinity conditions. At the same time, the best inversion model for autumn could also be applied for the SSC inversion in summer and was

5   selected as the optimal SSC model for autumn and summer in the study region.

In the YRD region, the spatial distribution of SSC shows a gradually increasing trend from southwest to northeast. The seasonal dynamics of SSC are such that soil salts accumulate in spring, decrease in summer, increase in autumn, and peak in winter.

10   These results are consistent with the results of field sampling, which showed that the SSC is highest in winter, followed by spring and autumn, and lowest in summer.

Author contributions. Hongyan Chen analyzed the data and prepared the manuscript. Gengxing Zhao developed the framework for the study. Danyang Wang and Ying Ma collected and

15   analyzed the data. Yuhuan Li provided technical support throughout different stages of the study. All coauthors provided a manuscript review.

Competing interests. The authors declare that they have no conflict of interest.

Acknowledgments

20   This work was financially supported by the National Natural Science Foundation of China, under grant numbers 41877003 and 41671346; the National Science and Technology Support Program of China, under grant number 2015BAD23B0202; the Funds of Shandong "Double

Tops" Program, under grant number SYL2017XTTD02; and Shandong Province key R & D

Plan of China, under grant number 2017CXGC0306.

References

5   Abbas, A., Khan, S., Hussain, N., Hanjra, M. A., and Akbar, S.: Characterizing Soil
        Salinity in Irrigated Agriculture using A Remote Sensing Approach. Physics and
        Chemistry of the Earth Parts, A/B/C55–57, 43–52. doi:
        10.1016/j.pce.2010.12.004, 2013.

    Ahmed, Z., and Iqbal, J.: Evaluation of Landsat TM5 Multispectral Data for Automated
10   Mapping of Surface Soil Texture and Organic Matter in GIS. European Journal
        of Remote Sensing, 47(1), 557-573. doi: 10.5721/EuJRS20144731, 2014.

    Allbed, A., Kumar, L., and Aldakheel, Y.Y.: Assessing Soil Salinity using Soil Salinity
        and Vegetation Indices derived from IKONOS High-spatial Resolution
        Imageries Applications in A Date Palm Dominated Region. Geoderma, 230–231,
15   1–8. doi: 10.1016/j.geoderma.2014.03.025, 2014.

    Allbed, A., and Kumar. L.: Soil Salinity Mapping and Monitoring in Arid and Semi-arid
        Regions using Remote Sensing Technology: A Review. Advances in Remote
        Sensing, 2, 373–385. doi: 10.4236/ars.2013.24040, 2013.

    Dehni, A., and Lounis. M.: Remote Sensing Techniques for Salt Affected Soil Mapping:
20   Application to the Oran Region of Algeria. Procedia Engineering, 33, 188–198.
        doi: 10.1016/j.proeng.2012.01.1193, 2012.

    Dwivedi, R.S., Kothapalli, R.V., and Singh. A. N.: Generation of Farm-level
        Information on Salt-affected Soils using IKONOS-II Multispectral Data. Remote
        Sensing of Soil Salinization: Impact on Land Management. CRC Press, Taylor
25   and Francis, New York, 73–89. doi: 10.1201/9781420065039.ch5, 2008.

    Elmetwalli, A. M. H., A. N. Tyler, P. D. Hunter, and C. A.: Salt Detecting and
        Distinguishing Moisture-and Salinity-induced Stress in Wheat and Maize
        through in Situ Spectroradiometry Measurements. Remote Sensing Letter 3:
        363–372. DOI: 10.1080/01431161.2011.599346, 2012.

30 Goto, K. , Goto, T. , Nmor, J. C. , Minematsu, K. , and Gotoh, K. . Evaluating Salinity
        Damage to Crops Through Satellite Data Analysis: Application to Typhoon

Affected Areas of Southern Japan. Natural Hazards, 75(3), 2815-2828. doi: 10.1007/s11069-014-1465-0, 2015.

Guo, Y., Shi, Z., Zhou, L. Q., Jin, X., Tian, Y. F., and Teng. H. F.: Integrating Remote Sensing and Proximal Sensors for the Detection of Soil Moisture and Salinity Variability in Coastal Areas. Journal of Integrative Agriculture, 12, 723–731. doi: 10.1016/S2095-3119(13)60290-7, 2013.

He, B., Cai, Y.L., Ran, W.R.,and Jiang. H.: Spatial and Seasonal Variations of Soil Salinity following Vegetation Restoration in Coastal Saline Land in Eastern China. Catena, 118, 147–153. doi: 10.1016/j.catena.2014.02.007, 2014.

Herrero, J., andCasta ñeda. C.: Temporal Changes in Soil Salinity at Four Saline Wetlands in NE Spain. Catena, 133, 145–156. doi: 10.1016/j.catena.2015.04.017, 2015.

Huang, J. Y., Shi, Z., and Biswas. A.: Characterizing Anisotropic Scale-specific Variations in Soil Salinity from A Reclaimed Marshland in China. Catena, 131, 64–73. doi: 10.1016/j.catena.2015.04.017, 2015.

Li, P., L. Jiang, and Z. Feng.: Cross-comparison of Vegetation Indices Derived from Landsat-7 Enhanced Thematic Mapper Plus (ETM) and Landsat-8 Operational Land Imager (OLI) Sensors. Remote Sensing 6: 310–329. doi: 10.3390/rs6010310, 2013.

Lu, Q. , Bai, J. , Fang, H. , Wang, J. , Zhao, Q. , and Jia, J.: Spatial and Seasonal Distributions of Soil Sulfur in Two Marsh Wetlands with Different Flooding Frequencies of the Yellow River Delta, China. Ecological Engineering, 96(96), 63-71. doi: 10.1016/j.ecoleng.2015.10.033, 2016.

Mahyou, H., Tychon, B., Balaghi, R., Louhaichi, M., and Mimouni. J.: A Knowledge-based Approach for Mapping Land Degradation in the Arid Rangelands of North Africa. Land Degradation & Development, 27, 1574–1585. doi: 10.1002/ldr.2470, 2016.

Mao, W. B., Kang, S. Z., Wan, Y. S., Sun, Y. X., Li, X. H., and Wang. Y. F.: Yellow River Sediment as a Soil Amendment for Amelioration of Saline Land in the Yellow River Delta. Land Degradation & Development, 27, 1595–1602. doi: 10.1002/ldr.2323, 2014.

Mehrjardi, R. T., Mahmoodi, S., Taze, M.,and Sahebjalal. E.: Accuracy Assessment of Soil Salinity Map in Yazd-Ar-dakan Plain, Central Iran, based on Landsat

ETM+ Imagery. American Eurasian Journal of Agricultural & Environmental Sciences, 3, 708–712, 2008.

Melendez-Pastor, I., Hernández, E. I., Navarro-Pedreño, J., and Gomez. I.: Mapping Soil Salinization of Agricultural Coastal Areas in Southeast Spain. Remote Sensing Applications, 6, 117–140. doi: 10.5772/36805, 2012.

Metternicht, G. I., and Zinck. J.A.: Remote Sensing of Soil Salinity: Potentials and Constraints. Remote Sensing of Environment, 85, 1–20. doi: 10.1016/S0034-4257(02)00188-8, 2003.

Rahmati, M., and Hamzehpour. N.: Quantitative Remote Sensing of Soil Electrical Conductivity using ETM+ and Ground Measured Data. International Journal of Remote Sensing, 38 (1), 123–140. doi: 10.1080/01431161.2016.1259681, 2016.

Scudiero, E., T. H. Skaggs, and D. L. Corwin.: Regional Scale Soil Salinity Assessment using Landsat ETM + canopy Reflectance. Remote Sensing of Environment, 169, 335–343. doi: 10.1016/j.rse.2015.08.026, 2015.

Shoshany, M., Goldshleger, N., and Chudnovsky. A.: Monitoring of Agricultural Soil Degradation by Remote-sensing Methods: A Review. International Journal of Remote Sensing, 34 (17), 6152–6181. doi: 10.1080/01431161.2013.793872, 2013.

Sidike, A., Zhao, S. H., and Wen. Y.M.: Estimating Soil Salinity in Pingluo County of China using Quick Bird Data and Soil Reflectance Spectra. International Journal of Applied Earth Observation and Geoinformation, 26, 156–175. doi: 10.1016/j.jag.2013.06.002, 2014.

Sturari, M., Frontoni, E., Pierdicca, R., Mancini, A., Malinverni, E. S., Tassetti, A. N., and Zingaretti, P.: Integrating Elevation Data and Multispectral High-resolution Images for an Improved Hybrid Land Use/Land Cover Mapping. European Journal of Remote Sensing, 50(1), 1-17. doi: 10.1080/22797254.2017.1274572, 2017.

Taghizadeh-Mehrjardi, R., Minasny, B., Sarmadian, F.,and Malone. B.: Digital Mapping of Soil Salinity in Ardakan Region, Central Iran. Geoderma, 213, 15–28. doi: 10.1016/j.geoderma.2013.07.020, 2014.

Tayebi, M. H., Tangestani, M. H., and Hasan Roosta. M. H.: Mapping Salt Diapirs and Salt Diapir-affected Areas using MLP Neural Network Model and ASTER Data.

International Journal of Digital Earth, 6, 143-157. doi: 10.1080/17538947.2011.606336, 2013.

Weng, Y. L., Gong, P.,and Zhu. Z. L.: A Spectra Index for Estimating Soil Salinity in the Yellow River Delta region of China using EO-1 Hyperion Data. Pedosphere, 20, 378–388. doi: 10.1016/S1002-0160(10)60027-6, 2010.

Wu, W. C., Mhaimeed, A.S., Al-Shafie, W.M., Ziadat, F., Dhehibi, B., Nangia, V., and Pauw. E. D.: Mapping Soil Salinity Changes using Remote Sensing in Central Iraq. Geoderma Regional, 2–3, 21–31. doi: 10.1016/j.geodrs.2014.09.002, 2014.

Yang, L., Huang, C., Liu, G.C., Liu, J., and Zhu. A. X.: Mapping Soil Salinity using A Similarity-based Prediction Approach: A Case Study in Yellow River Delta, China. Chinese Geographical Science, 25, 283–294. doi: 10.1007/s11769-015-0740-7, 2015.

Yang, S.Q., Zhao, W.W., Liu, Y.X., Wang, S., Wang, J., Zhai, R.J.: Influence of Land Use Change on the Ecosystem Service Trade-offs in the Ecological Restoration Area: Dynamics and Scenarios in the Yanhe Watershed, China. Science of the Total Environment, 644: 556–566. doi: 10.1016/j.scitotenv.2018.06.348, 2018.

Yu, R., Liu, T. X., Xu, Y. P., Zhu, C., Zhang, Q., Qu, Z.Y., Liu, X.M., and Li. C.Y.: Analysis of Salinization Dynamics by Remote Sensing in Hetao Irrigation District of North China. Agricultural Water Management, 97, 1952–1960. doi: 10.1016/j.agwat.2010.03.009, 2010.

Zhao, W.W., Wei, H., Jia, L.Z., Zhang, X., Liu, Y.X.: Soil Erodibility and its Influencing Factors on the Loess Plateau of China: A Case Study in the Ansai Watershed. Solid Earth, 9, 1507–1516, 2018.

Tables

Table 1. SSC descriptive statistics of samples and inversion

	Seasons	Minimum (g/kg)	Maximum (g/kg)	Mean (g/kg)	Standard deviation (g/kg)	Coefficient of variation	Sample points
Soil samples SSC	Spring	1.10	46.70	8.60	11.50	1.34	92
	Summer	1.34	29.20	5.32	5.95	1.12	30
	Autumn	0.90	36.70	7.80	8.20	1.05	110
	Winter	2.00	61.50	9.50	12.00	1.26	56
Inversion SSC	Spring	0.86	53.44	8.79	10.26		
	Summer	1.00	35.50	7.00	4.18		
	Autumn	0.82	35.15	8.28	9.21		
	Winter	1.12	58.10	9.21	13.78		

Table 2. Inversion models of SSC with IVIs from Landsat data

Modeling methods	Spring					Autumn				
	Calibration set		Validation set			Calibration set		Validation set		
	R^2	RMSE (g/kg)	R^2	RMSE (g/kg)	*RPD*	R^2	RMSE (g/kg)	R^2	RMSE (g/kg)	*RPD*
SMLR	0.42	9.03	0.62**	6.83	1.36	0.65**	3.42	0.56	3.81	2.01
BPNN	0.60**	7.56	0.57**	7.30	1.47	0.72**	3.39	0.68**	3.38	2.15
SVM	0.72**	6.34	0.71**	6.00	1.66	0.75**	3.48	0.78**	3.02	2.56

5   Significance levels: [**] 0.01

Table 3. Application of the best SSC inversion models

	The best inversion model for spring		The best inversion model for autumn	
	R^2	RMSE (g/kg)	R^2	RMSE (g/kg)
Summer samples (30)	0.23	5.31	0.65**	3.60
Winter samples (56)	0.66**	7.57	0.28	10.98

Significance levels: [**] 0.01

Table 4. The pixel number and proportion of pixels per SSC grade in four seasons

Grades	Spring		Summer		Autumn		Winter	
	Pixel number	Proportion %	Pixel number	Proportion %	Pixel number	Proportion %	Pixel number	Proportion %
Nonsaline soil (<2.0 g/kg)	10705	0.67	16	0	46439	2.89	3	0
Mild saline soil (2.0~4.0 g/kg)	84805	5.29	450331	28.07	127262	7.93	12	0
Moderate saline soil (4.0~6.0 g/kg)	451291	28.13	427216	26.63	182589	11.37	13045	0.81
Severe saline soil (6.0~10.0 g/kg)	597607	37.25	371641	23.16	305762	19.05	1294867	80.71
Solonchak (>10.0 g/kg)	459989	28.67	355193	22.14	942345	58.70	296470	18.48

Figures
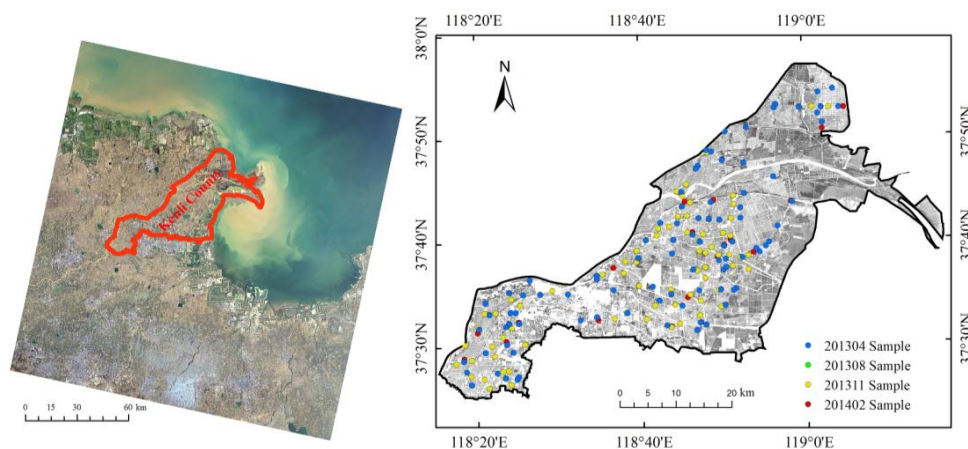
Figure 1. Location of the study area and sampling points
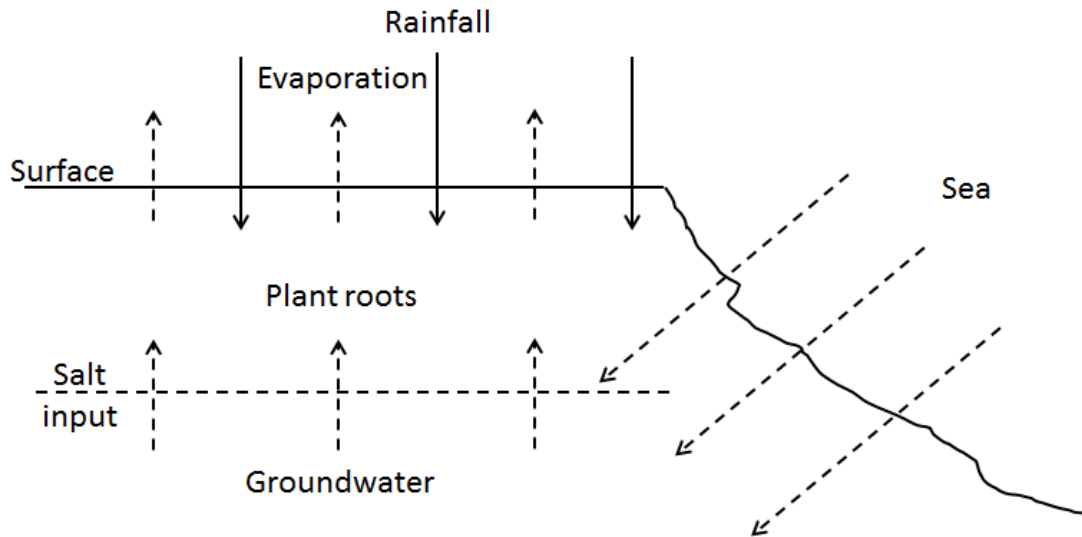
Figure 2. Soil salinization process in the study area
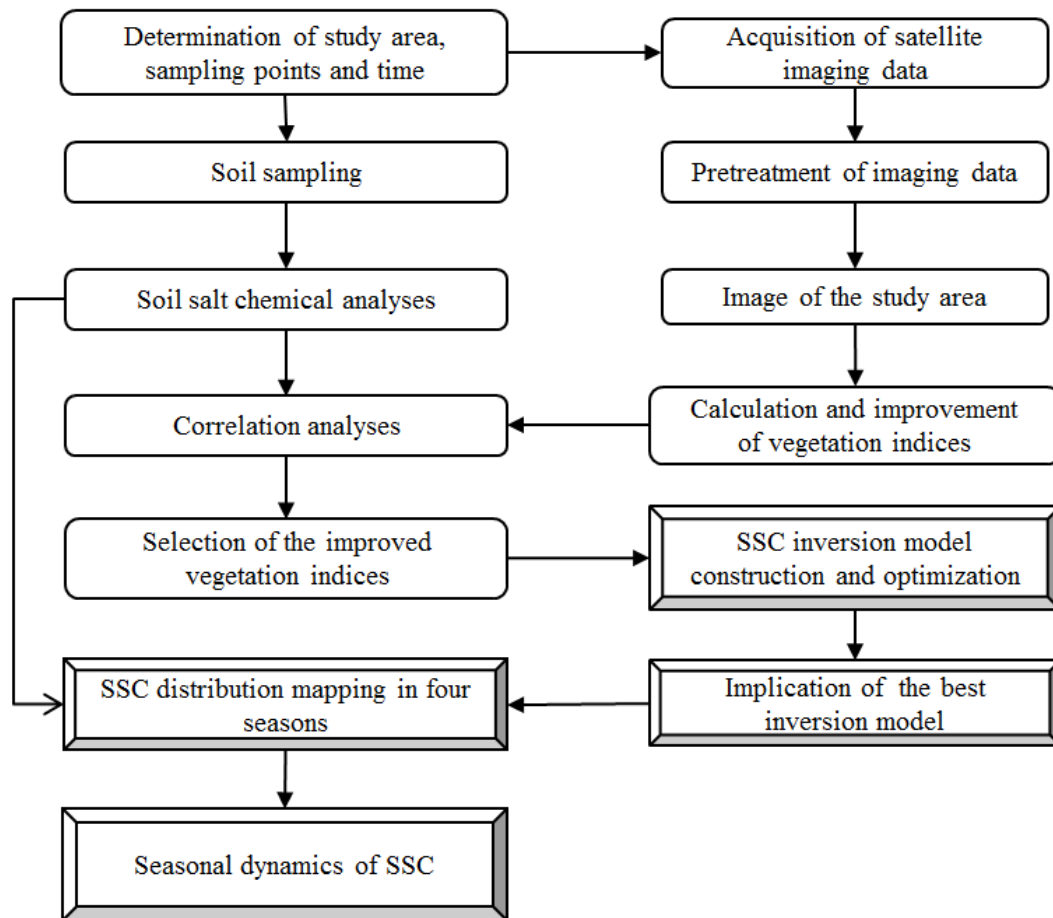
5   Figure 3. The methodological flow chart
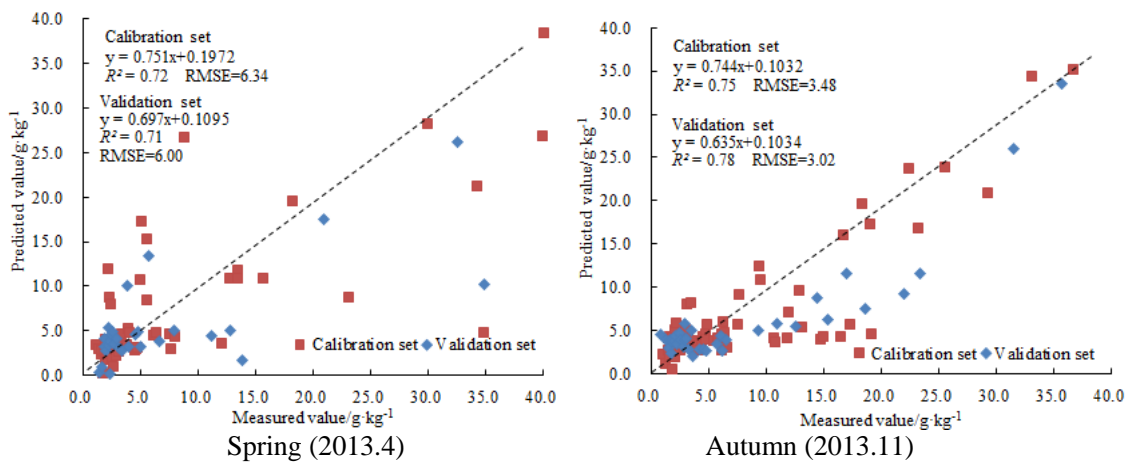
Figure 4. The calibration and validation precision of SSC inversion models in spring

5   and autumn
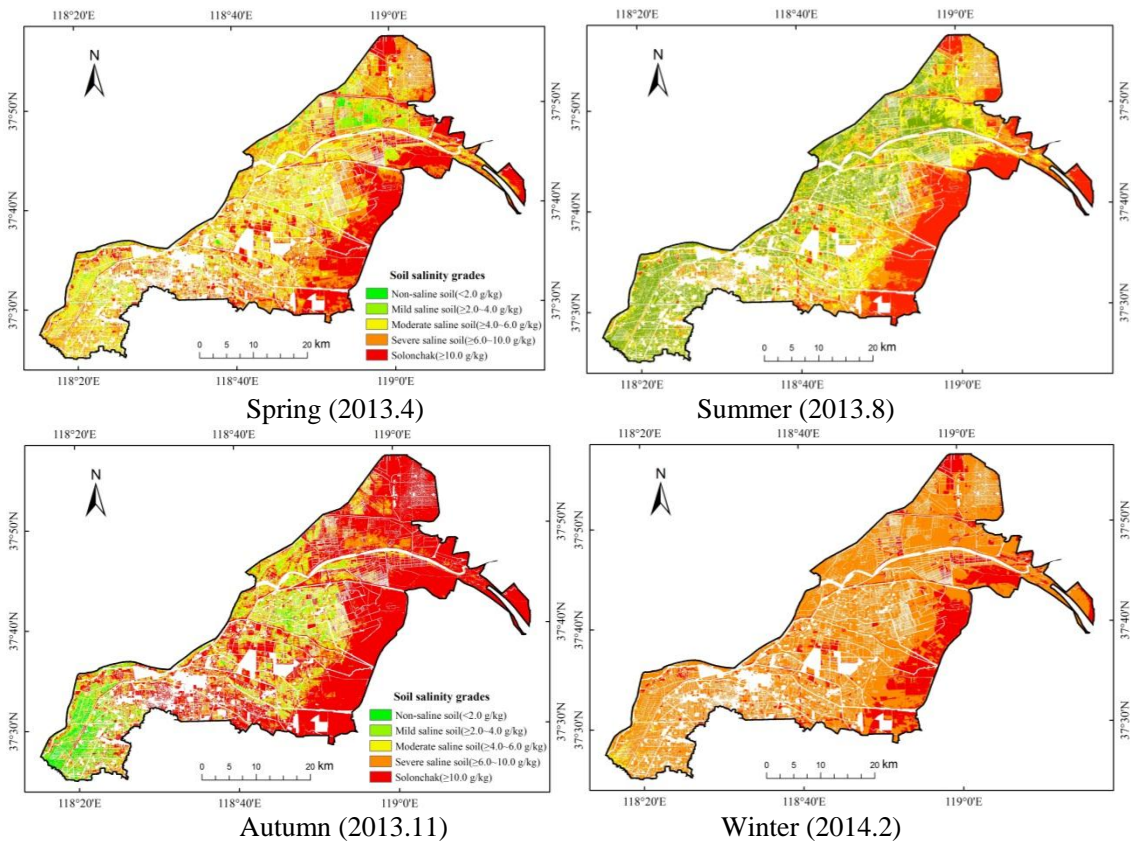
Figure 5. The inversion and distribution of SSC in four seasons